Electronic Supplementary Material (ESI) for Journal of Materials Chemistry C.

High-pressure ilmenite-type $MnVO_3$: crystal and spin structures in the itinerant-localized regimes.

Elena Solana-Madruga,[a, b] Olivier Mentré,[a] Eugenia P. Arévalo-López, [c] Dmitry Khalyavin, [d] Francois Fauth[e], Alexandr Missiul[e] and Angel M. Arévalo-López.*[a]

[a] UMR-8181-UCCS- Unité de Catalyse et Chimie du Solide -Univ. Lille, CNRS, Centrale Lille, ENSCL, Univ. Artois, F-59000 Lille, France. *angel.arevalo-lopez@univ-lille.fr.

[b] Dpto. Q. Inorgánica, Facultad CC. Químicas, Universidad Complutense de Madrid, Avda. Complutense sn, 28040, Madrid, Spain.

[c] Facultad de Ciencias, Universidad Nacional Autónoma de México, A.P. 70-399, Cd. México 04510, México.

[d] ISIS Facility, Rutherford Appleton, Laboratory, Harwell, Oxford, Didcot OX11 0QX, United Kingdom.

[e] CELLS-ALBA synchrotron, Carrer de la Llum 2-26, 08290, Cerdanyola del Vallés, Barcelona, Spain.

* angel.arevalo-lopez@univ-lille.fr

Experimental details:

High-pressure Synthesis.

The control on the high pressure and high temperature synthesis conditions reported in the main text of this article are automated. Pressure was calibrated following standard methods,[1-3] using well-known structural-electrical transitions for reference materials including Bi, ZnTe, ZnS and GaAs. In all cases, a two-probe method was used to measure electrical resistivity on the reference samples. Relating the oil pressure with the reference values for each transition, a calibration curve was extracted for daily automated control on pressure increase to target values. Additional calibration runs included the study of the well-known and reproducible structural phase transition of SiO_2 coesite-stishovite phases. For synthesis, pressure is increased to the target point, hold for the heating time with five mins stabilization before and after heating for safety and stability reasons. After this time, pressure is slowly released.

For temperature calibration, a C-type thermocouple (WRe alloys with 5% *vs.* 26% W) was used. The thermocouple is introduced next to the sample capsule and the required electrical power for several T steps is registered on heating at selected stable pressures. Although a thermocouple is used for every experiment, having a T-calibration is useful in case of accidental thermocouple break and for setting automated parameters for heating from power control. Regarding the accuracy of the temperature, the standard tolerance of a C-type thermocouple in the experimental temperature range is of ±1%, i.e. ± 10 K, which is negligible in the context of a quenched sample.

Detailed studies on how pressure affects temperature measurements using WRe thermocouples, [4] demonstrate this sensitivity raises the temperature reading tolerance to ± 30 K at pressures up to 16 GPa. Since our pressure synthesis is four times lower, it is reasonable to assume that the temperature difference of our reading cannot exceed this limit.

XPS spectroscopy.

We performed high resolution XPS spectra core level for Mn *2p*, V *2p* and O *1s* orbitals, the deconvolution is shown in Figure 2. Table S1 shows the binding energies for each orbital. Mn $2p_{1/2}$ and Mn $2p_{3/2}$ are located at 653.21 eV and 641.45 eV, respectively. According to references [5-7]. Mn^{2+} show characteristic shake-up satellites located at 659.14 and 647. 43 eV, Figure 2. The BE of Mn $2p_{3/2}$ core level indicates an oxidation state of Mn^{2+} [8, 9]. The BE of V $2p_{3/2}$ and V $2p_{1/2}$ are 515.78 and 523.35 eV, respectively. The BE obtained for V *2p* indicate an oxidation of 4+, in agreement with other reports [10,11].

X-ray photoelectron spectroscopy analyses were carried out in an ultra-high vacuum (UHV) system Scanning XPS microprobe PHI 5000 VersaProbe II, with an Al K□ X-ray source (hν= 1486.6 eV) monochromatic with 200 μm beam diameter, and a Multi-Channel Detector (MCD) analyzer. The surface of the sample was etched 5 min with 1 kV Ar^+ at 0.25 mA/mm². The XPS spectra were obtained at 45° to the normal surface with Constant Analyzing Energy (CAE) E_0 = 117.40 and 11.75 eV survey surface and high-resolution narrow scan. The peak positions were referenced to the background Ag $3d_{5/2}$ photopeak at 368.20 eV, with an FWHM of 0.56 eV, and C *1s* hydrocarbon groups at 285.00 eV, Au $4f_{7/2}$ at 84.00 eV central peak core level position. The XPS spectrum was fitted with the program MultiPak PHI software [12] and Spectral Data Processor, SDP v 4.1 [13].

Supplementary Figures:

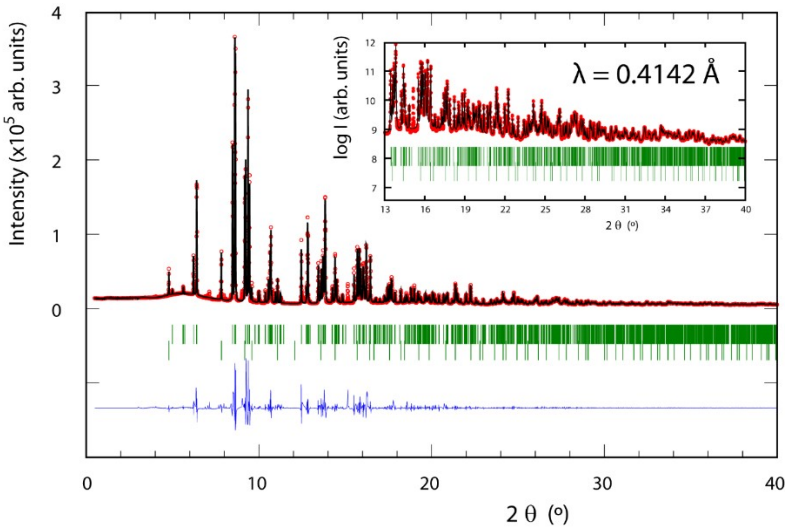

Fig. S1. Rietveld fit of the triclinic distorted (*P*-1) ilmenite structure of $MnVO_3$ – I against SXRD data collected at 560 K. Secondary minority phase MnV_2O_4 spinel (14%) is included in the second row of Bragg ticks.

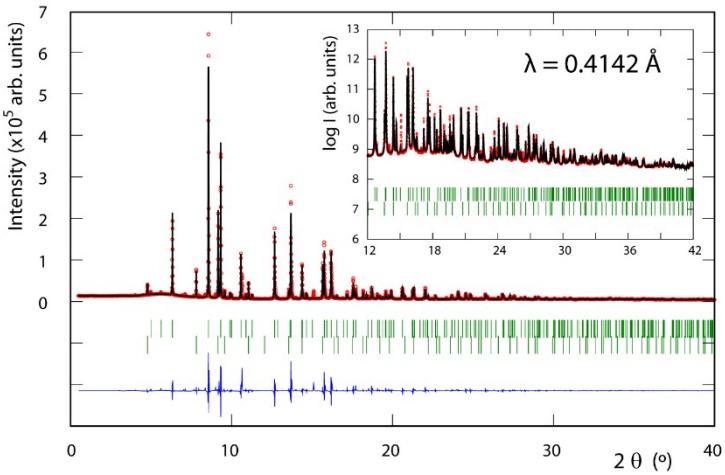

Fig. S2. Rietveld fit of the rhombohedral non-distorted (*R*-3) ilmenite structure of $MnVO_3$ – I against SXRD data collected at 560 K. Second rows of Bragg ticks are MnV_2O_4 (13.89%).

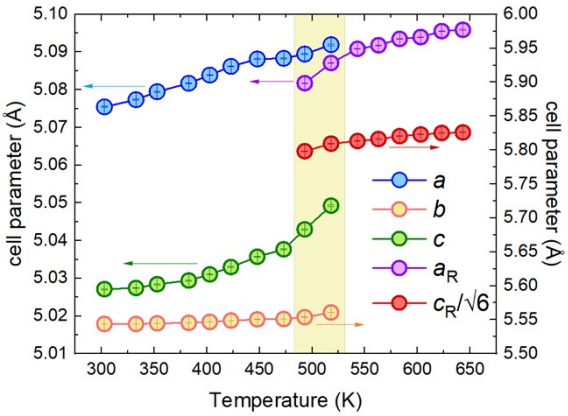

Fig. S3. Thermal evolution of lattice parameters in $MnVO_3$ -I in the 300 – 650 K temperature range, as refined from SXRD data. Phase transition from triclinic to rhombohedral structures, clear from abrupt change in the parameters, is identified by the shaded area.

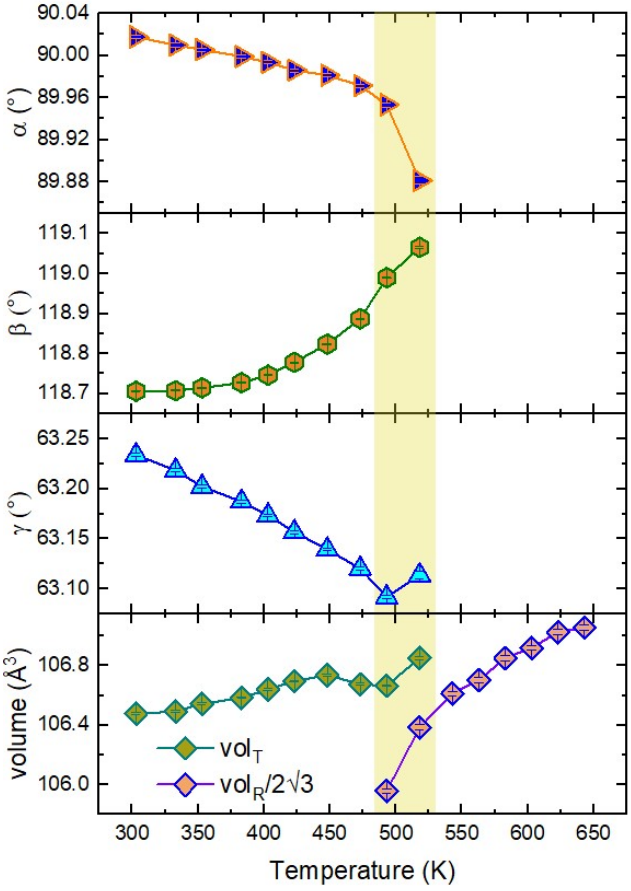

Fig. S4. Thermal evolution of unit cell angles and volume in $MnVO_3$ -I in the 300 – 650 K temperature range, as refined from SXRD data. Phase transition from triclinic to rhombohedral structures is identified by the shaded area.

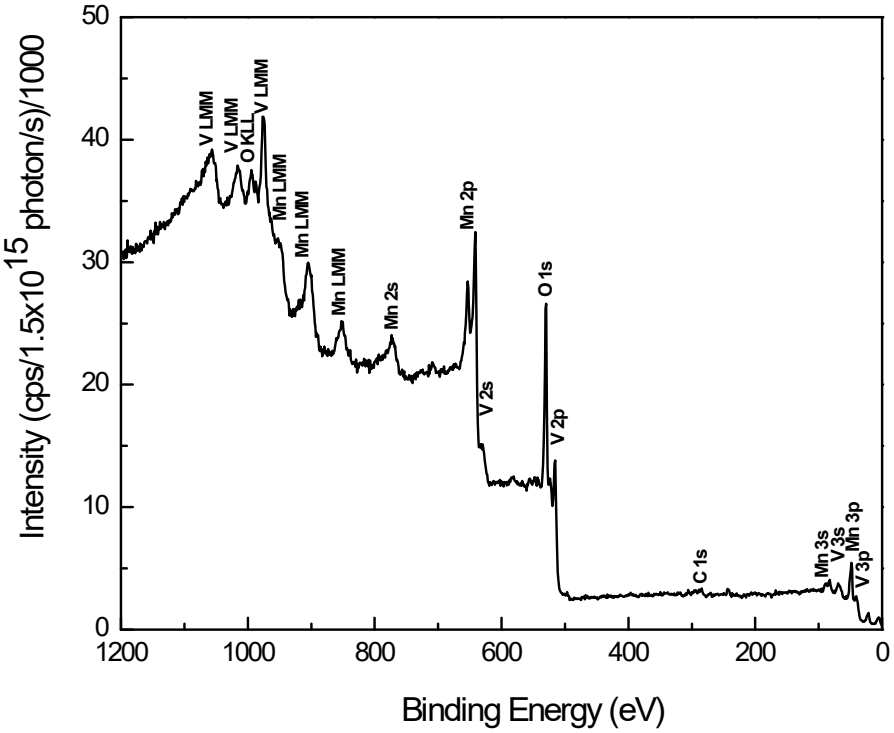

Figure S5 shows the X-ray photoelectron spectroscopy survey spectrum taken after etching the surface for 5 min with Ar^+ ions. Auger lines for Mn, V and O are observed at high binding energy (BE). At lower energies the characteristic orbitals for Mn, V and O are shown.

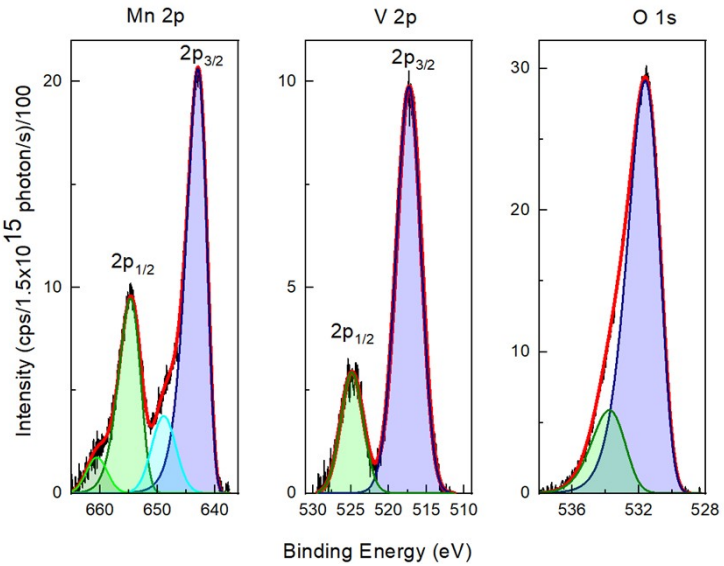

Figure S6. High resolution XPS spectra of Mn *2p*, V *2p* and O *1s* orbitals.

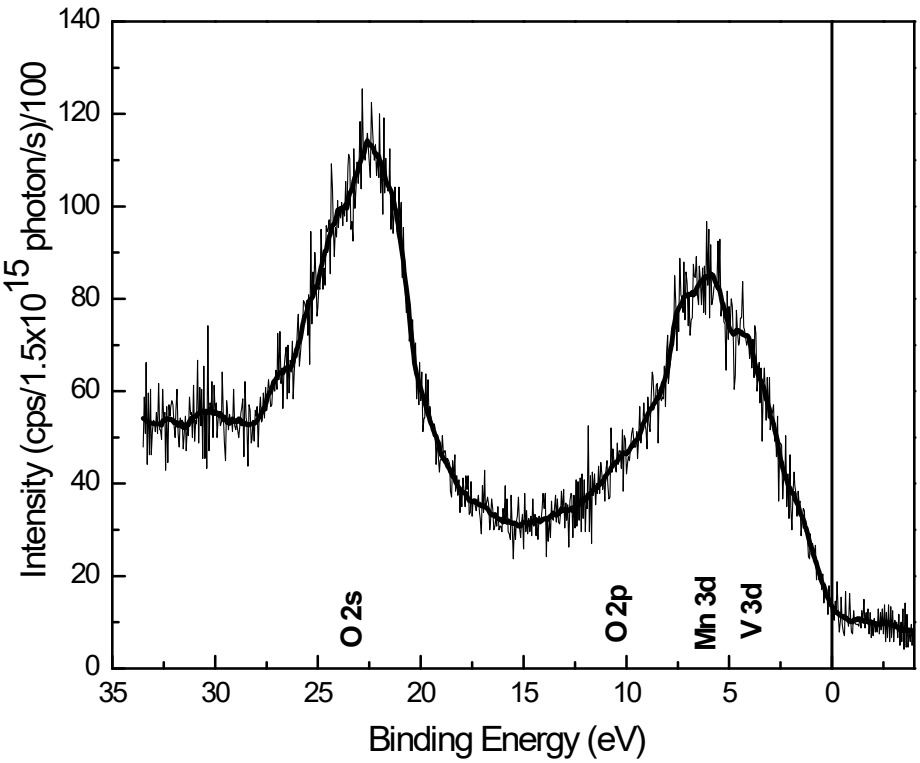

Figure S7 shows the XPS valence band spectra of $MnVO_3$. Near the Fermi level the contribution to the valence band comes from Mn *3d* and V *3d* orbitals. The continuous line shows the Fermi energy at zero eV. The valence band intensity at zero eV decreases suggesting a semiconductor behavior.

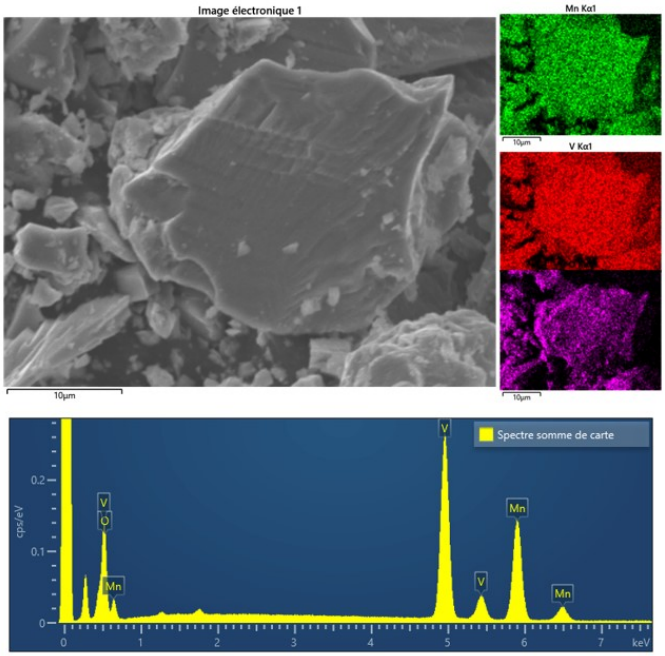

Figure S8 shows the Energy Dispersive X-ray Spectroscopy analysis of $MnVO_3$. The semiquantitative analysis results in a Mn/V = 1.1(1) ratio, in agreement with the composition.

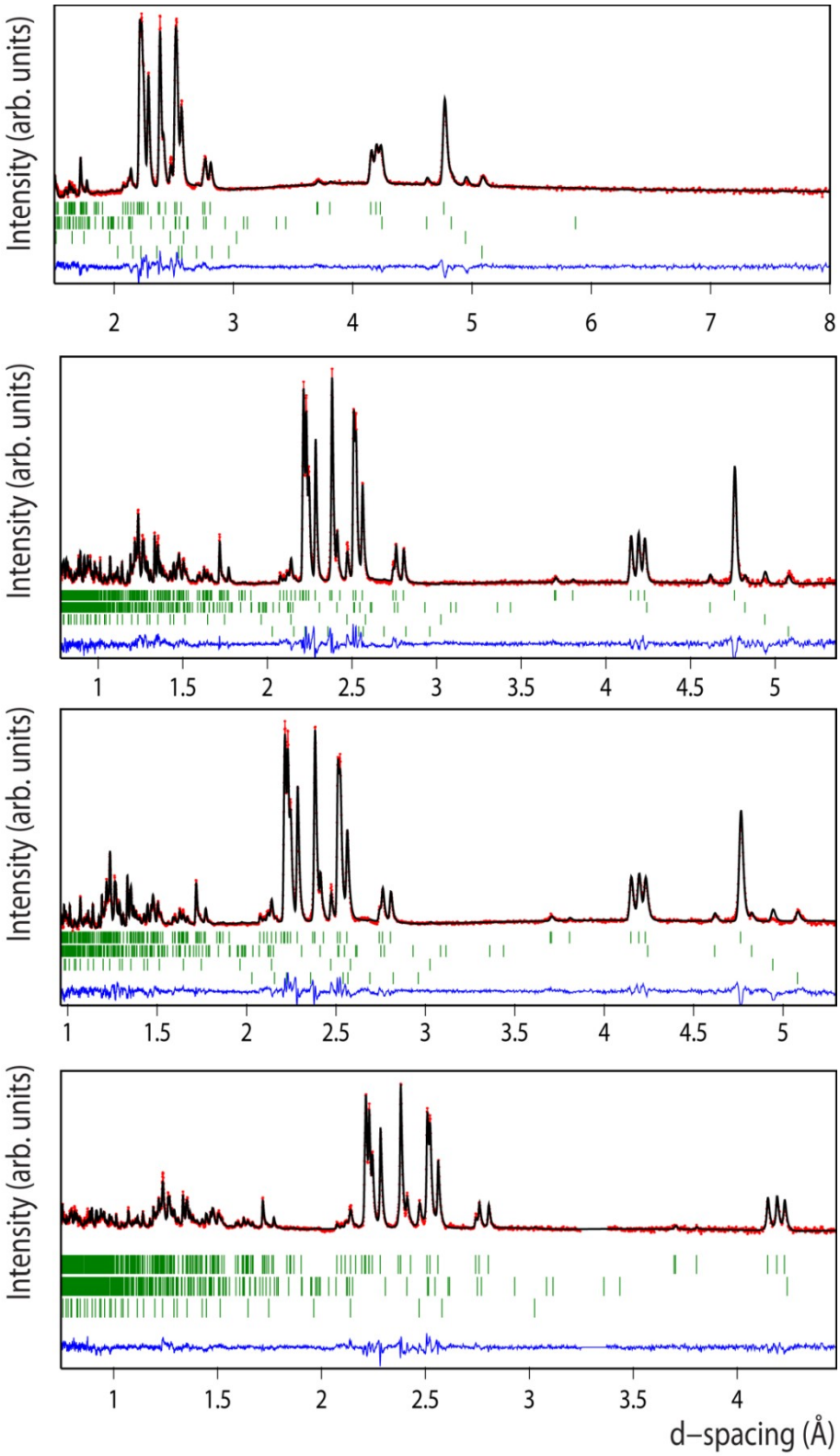

Fig. S9. Rietveld fits of the triclinic (*P*-1) ilmenite structure of $MnVO_3$ – I against NPD data collected at 100 K. First and second rows of Bragg ticks identify the main phase (nuclear and magnetic). Minor phases include $Mn_3V_2O_8$ (4.5%), MnV_2O_4 (2.5%) and magnetic MnO.

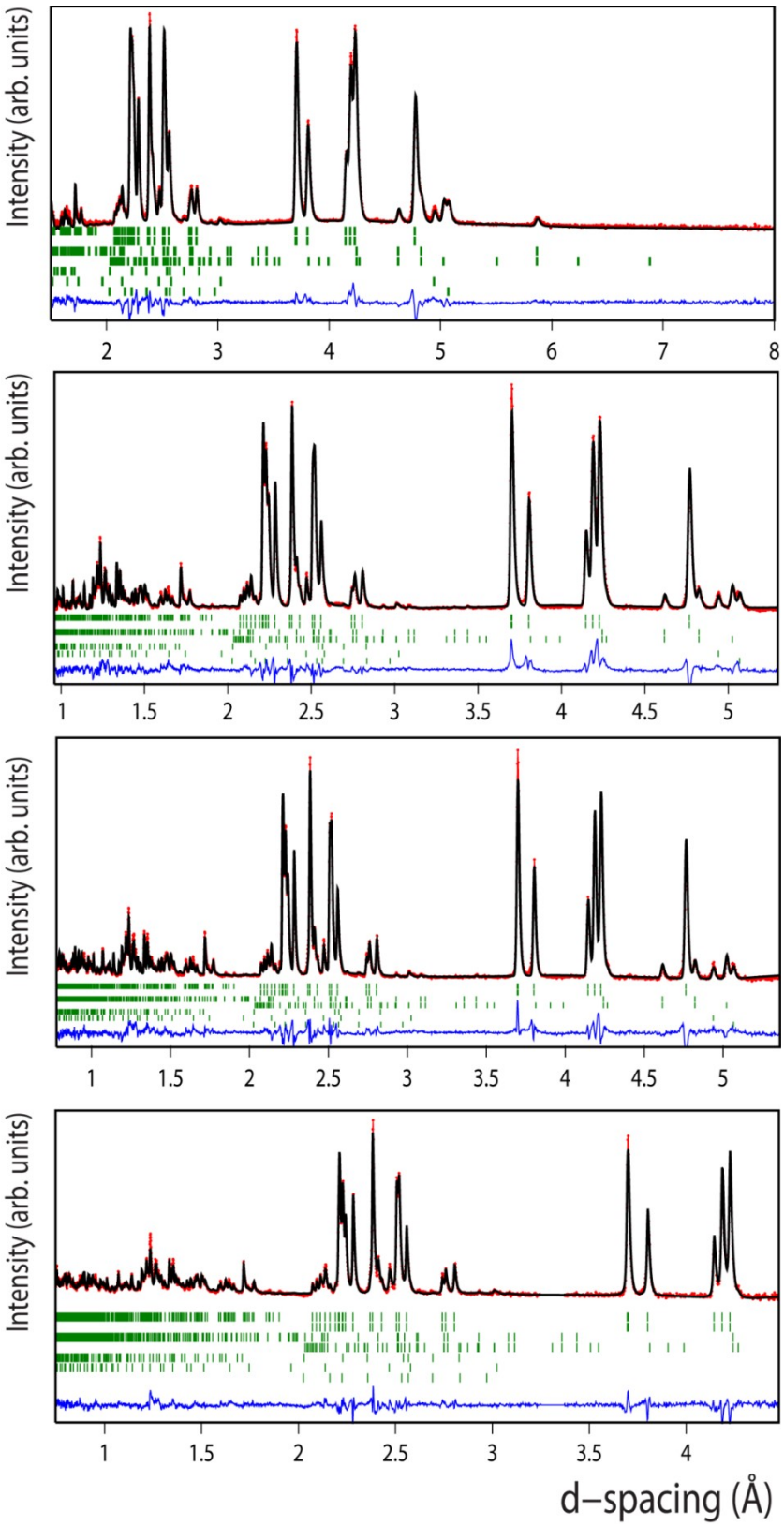

Fig. S10. Rietveld fits of the triclinic (*P*-1) ilmenite structure of $MnVO_3$ – I against NPD data collected at 2 K. First and second rows of Bragg ticks identify the main phase (nuclear and magnetic). Minor phases include $Mn_3V_2O_8$ (4.5%), MnV_2O_4 (2.5%) and magnetic MnO.

Supplementary Tables:

Table S1. Atomic positions (top) and anisotropic thermal factors (bottom) of $MnVO_3$ – I, refined from 300 K single crystal XRD data. Space group *P*-1 and cell parameters *a* = 5.0177(7) Å, *b* = 5.0513(7) Å, *c* = 5.5210(8) Å, *α* = 116.679(6) °, *β* = 90.044(6) ° and *γ* = 118.924(5) °.

Site	x	y	z	Occ
Mn (2i)	0.64890(12)	0.28595(15)	0.42166(13)	1
V (2i)	-0.14533(13)	-0.28822(17)	0.04681(15)	1
O1 (2i)	0.5762(6)	-0.2169(7)	0.2255(6)	1
O2 (2i)	0.2209(5)	0.1673(7)	0.2342(6)	1
O3 (2i)	0.9684(6)	0.5195(7)	0.2315(6)	1

Site	U_{11} (Å^2)	U_{22}(Å^2)	U_{33}(Å^2)	U_{12}(Å^2)	U_{13}(Å^2)	U_{23}(Å^2)
Mn (2i)	0.0106(4)	0.0090(4)	0.0082(4)	0.0060(3)	0.0015(3)	0.0044(4)
V (2i)	0.0088(4)	0.0061(4)	0.0043(4)	0.0052(3)	0.0014(3)	0.0019(3)
O1 (2i)	0.0128(12)	0.0090(15)	0.0080(15)	0.0084(11)	0.0025(10)	0.0032(14)
O2 (2i)	0.0102(12)	0.0062(14)	0.0070(15)	0.0025(10)	-0.0004(10)	0.0026(14)
O3 (2i)	0.0095(12)	0.0080(14)	0.0060(14)	0.0054(10)	0.0013(10)	0.0033(13)

Table S2. Crystal data and structure refinement information for $MnVO_3$ – I at 300 K, space group *P*-1.

Molar mass (g mol^{-1})	153.9
Unit cell dimensions (Å)	a = 5.0177(7), b = 5.0513(7), c = 5.5210(8)
Unit cell angles (°)	α = 116.679(6), $\beta = 90.044(6)$, $\gamma = 118.94(5)$
Unit cell volume (Å^3)	105.10(3)
Calculated density (g cm^{-3})	4.8621
Wavelength	Ag *Kα* (0.56086 Å)
Absorption coefficient (mm^{-1})	5.185
F(000)	144
Θ range / °	3.39 to 23.66
hkl range	-7 ≤ *h* ≤ 7, -7 ≤ *k* ≤ 6, -7 ≤ *l* ≤ 7
Total no. reflections	604
Independent refelctions	544
Data/parameters	544 / 47
Goodness of fit on F^2	2.63
R1/wR2 (I ≥ 3σ)	0.0318 / 0.0452
R1/wR2 (All data)	0.0318 / 0.0452
Largest diff. peak and hole (e$^-$ A^3)	1.75 / -0.72

Table S3. Atomic positions and main interatomic distances of $MnVO_3$ – I, refined from the 560 K SXRD data. Space group *R*-3 and cell parameters *a* = 5.09411(8) Å, *c* = 14.2551(3) °. Agreement factors: R_p = 5.39%, R_{wFp} = 14.85%, R_B = 8.39%, R_f = 6.65%, χ^2 = 5.60%

Site	x	y	z	Occ
Mn (2c)	0.0	0.0	0.1398(1)	1
V (2c)	0.0	0.0	0.3486(1)	1
O (6f)	0.294(1)	-0.029(3)	0.2570(6)	1

Bond Mn-O	Length (Å)	Bond V-O	Length (Å)
(Mn-O)x3	2.081(7)	(V-O)x3	1.87(1)
(Mn-O)x3	2.298(9)	(V-O)x3	2.048(9)

Table S4. Atomic positions and main interatomic distances of $MnVO_3$ – I, refined from the 2 K NPD data. Space group *P*-1 and cell parameters *a* = 5.01300(12) Å, *b* = 5.03998(14) Å, *c* = 5.53403(1) Å, *α* = 116.513(2) °, *β* = 89.920(3) ° and *γ* = 118.811(2) °. Agreement factors: R_p = 4.27%, R_{wp} = 5.52%, R_f = 6.22%, χ^2 = 9.25%

Site	x	y	z	Occ	U_{iso} (Å^2)
Mn (2i)	0.6497(1)	0.280(1)	0.418(1)	1	0.009(1)
V (2i)	-0.144(1)	-0.274(1)	0.061(1)	1	0.009(1)
O1 (2i)	0.5728(9)	-0.2221(1)	0.2179(9)	1	0.011(6)
O2 (2i)	0.2171(9)	0.166(1)	0.2338(9)	1	0.011(6)
O3 (2i)	0.9678(9)	0.5166(9)	0.2314(8)	1	0.011(6)

Bond Mn-O	Length (Å)	Bond V-O	Length (Å)
(Mn-O1)	2.365(9) / 2.076(9)	(V-O1)	1.733(9) / 2.170(6)
(Mn-O2)	2.087(9) / 2.317(8)	(V-O2)	1.829(6) / 2.022(10)
(Mn-O3)	2.074(8) / 2.196(8)	(V-O3)	1.942(11) / 2.038(9)

Table S5. Experimental binding energies (BE) of Mn *2p*, V *2p* and O *1s* orbitals of $MnVO_3$, compared to reference oxides.

Oxidation state	Orbital	BE (eV) this work	Oxide	BE (eV)	Ref.
Mn^{2+}	$2p_{1/2}$	653.21			
Mn^{2+}	$2p_{3/2}$	641.45	MnO	641.30-641.70	[4-5]
V^{4+}	$2p_{1/2}$	523.35			
V^{4+}	$2p_{3/2}$	515.78	VO_2	515.95-515.65	[6-7]
O^{2-}	*1s*	530.09			

References

[1] J. S. Knibbe, S. M. Luginbühl, R. Stoevelaar, W. van der Plas, D. M. van Harlingen, N. Rai, E. S. Steenstra, R. van de Geer and W. van Westrenen, *EPJ Techniques and Instrumentation,* 2018, **5**, 5.

[2] M. R. Schwarz, *J. Phys.: Conf. Series*, 2010, **215**, 012193.

[3] http://multianvil.asu.edu/MainPage_Cell.html

[4] Y. Nishihara, S. Doi, S. Kakizawa, Y. Higo and Y. Tange, *Physics of the Earth and Planetary Interiors*, 2020, **298**, 106348.

[5] M. Oku, K. Hirokawa and S. Ikeda, *J. Electron Spectrosc. Relat. Phenom.*, 1975, **7**, 465.

[6] V. D. Castro and G. Polzonetti, *J. Electron Spectrosc. Relat. Phenom.*, 1989, **48**, 117.

[7] C. Aguilar-Maldonado, E. P. Arévalo-López, C. Ritter, O. Mentré, A. M. Arévalo-López *Inorg. Chem*. 2020, **59**, 13128-13135.

[8] A. Aoki, *Jpn. J. Appl. Phys*., 1976, **15**, 305.

[9] J.C. Carver, G.K. Schweitzer and T.A. Carlson, *J. Chem. Phys.* 1972, **57**, 973.

[10] E. Hryha, E. Rutqvistband, and L. Nyborg, *Surf. Interface Anal.* 2012, **44**, 1022-1025.

[11] J. Mendialdua, R. Casanova, Y. Barbaux, *J. Electron Spectrosc. Relat.Phenom*.1995, **71**, 249.

[12] Multipack version 9.6.0.15, 2015-02-19, Ulvac-phi, Inc, Physical Electronics USA, 1994-2014.

[13] B. V. Crist, 17 January 2004 SDP v 4.1 (32 bit) Copyright ©□2004, XPS International, LLC, Compiled January 17, 2004. http://www.xpsdata.com